Chapter 6

A model of the austenitic MMA weld

In this chapter, the important example in ultrasonic NDT of an austenitic manual metal arc (MMA) weld is considered. Austenitic steels having a face-centered-cubic structure (as opposed to ferritic steels having a body-centered-cubic structure) solidify in large grains which can be up to several centimeters long [29]. This is in contrast with ferritic steels, which usually have grain sizes much less than a millimeter. These grains are furthermore randomly oriented, making ferritic steels homogeneous and isotropic for elastic waves at a few MHz. The large grains in solidified austenitic steel together with their non-random orientations makes such a weld highly inhomogeneous and anisotropic and may therefore present the operator or interpreter with great difficulties during the phase of analysis and interpretation of the gathered A-scan data. For this reason, a material model of the weld which may be incorporated into a simulation tool for the simulation of beam path and A-scans may prove extremely valuable.

In the first section, such a parametrized model as developed in [59] is presented and it is adapted to the numerical method developed in the previous chapter. In the second section, a number of simulations for different choices of weld parameters as well as transducer parameters will be shown.

6.1 A parametric model of the MMA austenitic weld

Fig. 6.1 shows the macrograph of an X 6 CrNi 18 11 austenitic MMA weld placed in ferritic steel. The weld is manually fabricated and consists of layers of beads placed side by side. The bead boundaries clearly show up as arcs in the figure, and it is seen that the weld consists of a large number of these. As the beads solidify, grains are formed with the long axis mainly in the direction of the temperature gradient. Each grain consists of a number of crystallites with a preferred crystal axis also in the direction of the temperature gradient. The preferred crystal axis is empirically known to be the [001] axis while the two other axes [100] and [010] are randomly oriented. This means, that each grain may be considered to be transversely isotropic with the symmetry axis along the temperature gradient. As this gradient varies smoothly from point to point, nearby grains have similar axis orientations rather than being random. For each new layer of beads added in the welding process, the layer below partly participates in the solidification process a second time with the result that grains may extend over several beads. The long axis of the grains show up in the figure as white lines with orientations depending on the position in the weld. The directions of a few of these lines are illustrated with solid lines in the left plot. Close to the two sloping boundary planes, the temperature gradient becomes more horizontal depending on the slopes of the two planes. This is also reflected in the plot for the solid lines near the boundaries. The right plot shows a magnification of the rectangular region in the right plot. The boundaries of the beads are clearly visible and it is shown, that grains may extend over several beads. In fact, the beads themselves are not believed to have any influence on ultrasound. The weld direction, i.e. the direction perpendicular

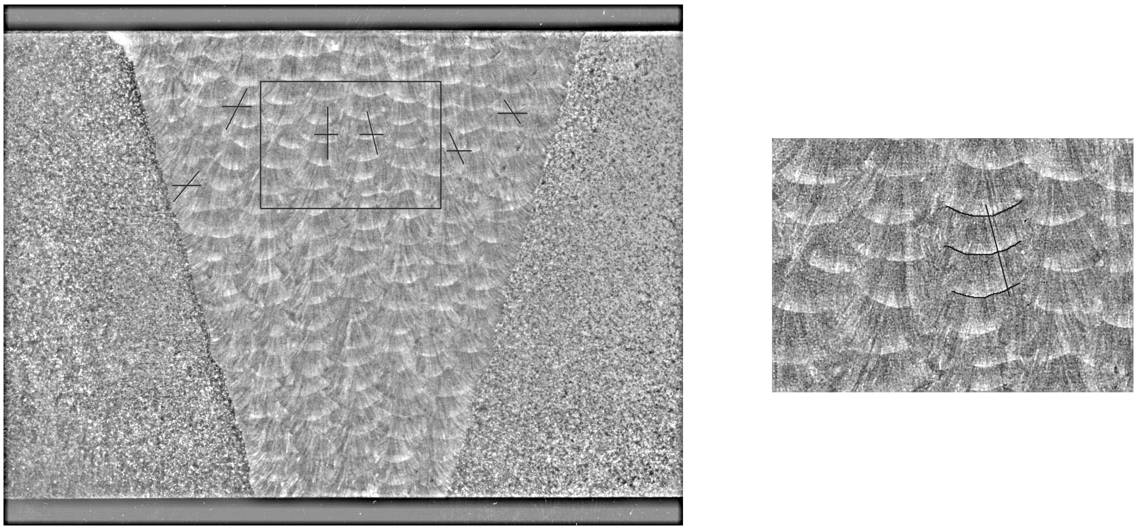

Figure 6.1: A macrograph (left) of the cross section of an austenitic X 6 CrNi 18 11 MMA weld in ferritic steel base metal. Outer dimensions are 60 mm (height) and 90 mm (length). Right plot is an enlargement of the rectangle on the left plot. Solid lines show the directions of the long grain axis at different positions.

to the cross section in Fig. 6.1 in which the weld is build, also has an influence on the long grain axis orientation through the temperature gradient. It is empirically known, that the long grain axis may point in the weld direction with an angle of up to 10°. This angle is called the *layback* angle.

The characteristics of the orientation of the long grain axis as described above and illustrated in the figure may be summarized as follows [59]

- the long grain axis is near vertical along the center of the weld.
- the weld may approximately be treated as symmetric with respect to a vertical plane through the center line, with the two opposite sloping boundary planes at equal and opposite angles.
- the long grain axis slope decreases with increasing distance from the centre of the weld.
- the long grain axis slope along the two sloping boundary planes is approximately constant.

- the rate of change of the symmetry axis direction with distance from the weld centre decreases away from the centre.

Based on these observations, an expression for the angle of the long grain axis or equivalently the symmetry axis in the weld as a function of position is set up with reference to Fig. 6.2. Other expressions describing the above observations may be constructed, but here we follow [59]. A x_1x_3-coordinate system is positioned at the midpoint of the bottom

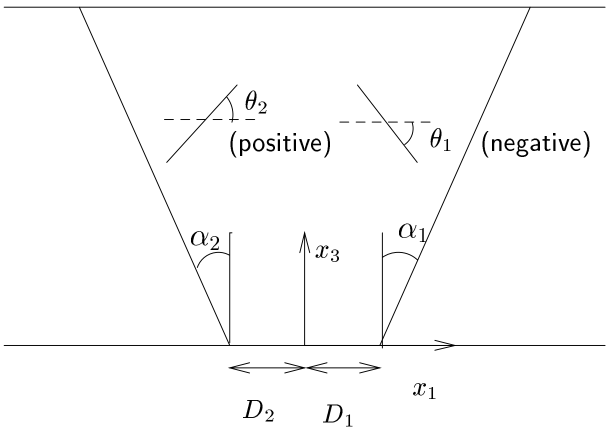

Figure 6.2: Illustration of the parameters entering the weld model.

line of the weld. For $x_1 > 0$, θ_1 denotes the (positive) angle between horizontal and the long grain axis, while for $x_1 < 0$, θ_2 denotes the (negative) angle between horizontal and the long grain axis, see Fig. 6.1. α_1 denotes the positive angle between vertical and the boundary plane with a similar definition for α_2. Finally, D_1 denotes the (positive) distance from the origin of the coordinate system to the boundary plane and with a similar definition for D_2. These parameters are all determined by the actual geometry of the weld considered. With these definitions in mind, the following expressions for the two angles θ_1 and θ_2 are suggested

$$\tan\theta_1(x_1, x_3) = -\frac{T_1(D_1 + x_3\tan\alpha_1)}{x_1^\eta}, \qquad x_1 > 0 \tag{6.1a}$$

$$\tan\theta_2(x_1, x_3) = \frac{T_2(D_2 + x_3\tan\alpha_2)}{|x_1|^\eta}, \qquad x_1 < 0 \tag{6.1b}$$

To be strictly correct, x_1 and x_3 as well as D_1 and D_2 on the right hand side of (6.1) have been made dimensionless through a division with unit length. In (6.1), two types of dimensionless hyper parameters T_1, T_2 and a positive η have been introduced. The parameter η controls the rate of change of the orientation of long grain axis across the weld. A high value results in a large rate of change towards a vertical orientation while a small value results in long grain orientations being nearly constant across the weld. The effect of T_i is best appreciated near the sloping boundary planes with $\eta = 1$, where the right hand sides of (6.1) equal T_i. For numerically large values of T_i, the grain orientations approach vertical while for small values of T_i, the orientations become horizontal. As an example, the introduced parameters have the measured values $D_1 = D_2 = 13\,\mathrm{mm}$ and $\alpha_1 = \alpha_2 = 17°$ for the weld in Fig. 6.1.

The effect of the parameters on the modelled grain axis orientations for different values are illustrated in a few plots in the following. The parameters D_i and α_i have values corresponding to the weld in Fig. 6.1. Fig. 6.3 shows the grain orientations for $T_1 = T_2 = 1.3$ (left) and $T_1 = T_2 = 0.6$ (right), and with the value $\eta = 1.0$ for both plots. The grain axis orientations are more horizontal in the right plot as expected. Fig. 6.4 shows the

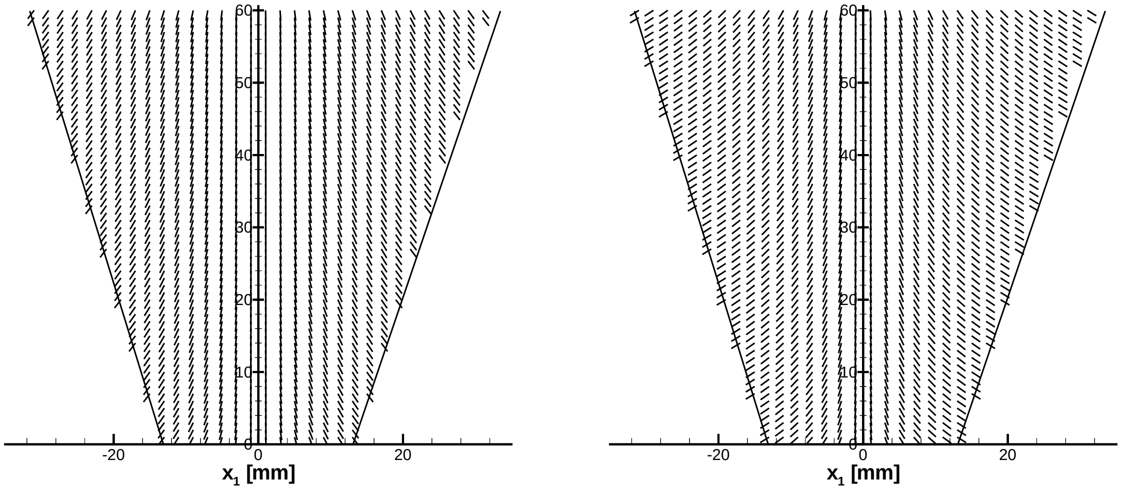

Figure 6.3: Modelled grain axis orientations for $T_1 = T_2 = 1.3$ (left) and $T_1 = T_2 = 0.6$ (right). In both cases $\eta = 1.0$.

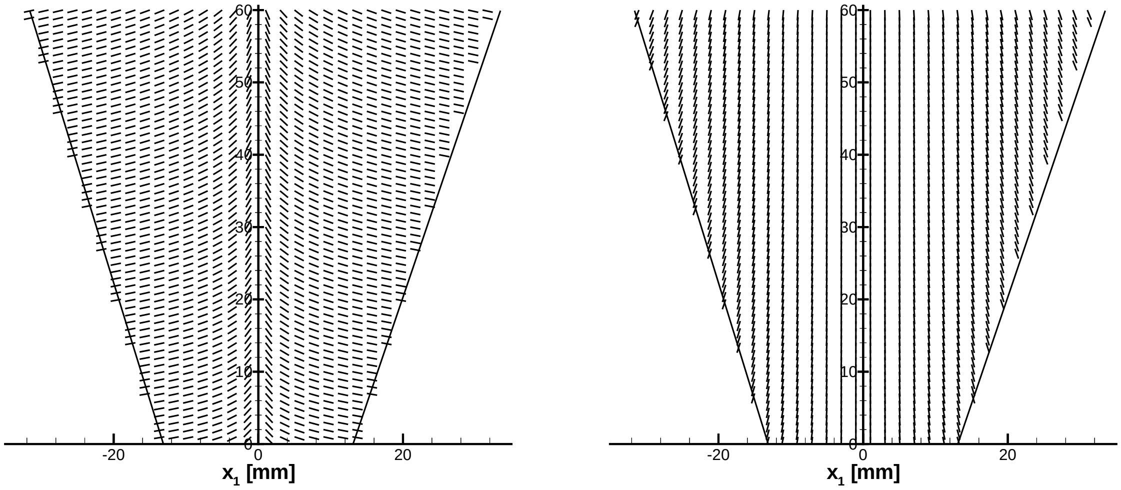

Figure 6.4: Modelled grain axis orientations for $\eta = 0.7$ (left) and $\eta = 1.4$ (right). In both cases $T_1 = T_2 = 0.6$.

grain orientations for $\eta = 1.0$ (left) and $\eta = 1.4$ (right), and with the value $T_1 = T_2 = 0.6$ for both plots. As expected, the rate of change of the grain axis orientations is much more pronounced in the right plot. The wave propagation through the weld in Fig. 6.1 has been studied experimentally as well as through a simulation as described in the next section.

As a final comment, the model (6.1) of the long grain axis orientations is a continuous model based on the empirical observations summarized above. The issues of the geometry and extent of the grains are not addressed. These important issues should in principle be dealt with separately.

6.2 Adapting the weld model to the numerical approach EFIT

The adaption of the weld model described in the previous section to the numerical approach EFIT is in principle straightforward. However, some approximations must be introduced, partly due to the restriction to a 2D formulation of the problem.

6.2.1 Adaption of the model

Due to the restriction to a 2D formulation of the problem, the energy should propagate entirely within the x_1x_3-plane. For an transversely isotropic medium this restricts the long grain axis (parallel to the crystal symmetry axis of the transversely isotropic material) to lie entirely in this plane. This follows directly from inspection of the slowness surface restricted to this plane as discussed in connection with Fig. 3.3. Thus, the layback angle is assumed to be zero. Concerning beam skewing, this is not a serious problem, as the out-of-plane energy propagation is not large compared to the in-plane energy propagation. However, in a real inspection situation, all three types of waves (qL, qT1 and qT2) will be excited, even for a piezoelectric transducer as shortly mentioned in section 3.2. For the present 2D problem, only two wave types (qSV and qL) are seen for a piezoelectric transducer at the surface.

The other issue is the relation between the material grid in the numerical approach and the grain size and geometry. A quadratic grid, see Fig. 4.5, is imposed on the weld and to each cell an elastic matrix (and a mass density) is attached. The orientation of the symmetry axis for each cell is found using (6.1) and the corresponding elastic matrix rotation relative to a fixed coordinate system is performed using (2.23). Thus, the grains in the weld are modelled as squares in 2D with dimensions equal to those of the grid cells (typically $0.1\,\mathrm{mm} \times 0.1\,\mathrm{mm}$), which is presumably not realistic.

6.2.2 Experiment and simulation: A review

A study [28] was carried out to determine the wave propagation through the weld in Fig. 6.1 experimentally as well as through a number of simulations with different choices of parameters using the above discretization of the weld model. Six copies of the weld piece shown in the figure were available. For each copy, the left vertical boundary of the specimen was machined so as to be parallel to the left weld boundary, making it possible to achieve normal incidence at the weld boundary using an unangled 2 MHz transducer. This is illustrated in Fig. 6.5 with the leftmost line indicating the cut. For each of the six copies the opposite vertical boundary was cut so as to be parallel to the left boundary. This was performed with increasing distances between the two parallel boundaries, as illustrated in the figure showing the six distances, ranging from 18.5 mm to 53.5 mm, between the parallel boundaries. By positioning a transmitter and a receiver on opposite parallel boundaries for each copy, it was thus possible to trace the sound through the weld. Simulations of the wave propagation through the weld were performed and the signals were recorded at the same positions as in the experiment. This was performed for different choices of parameter values. A best set of parameters, was picked based on a comparison with the experimental result. The set of values for the best match was $T = 1.3$ and $\eta = 1.0$ shown in Fig. 6.3 (left). The set of values for the worst match was $T = 0.6$ and $\eta = 0.7$ shown in Fig. 6.4 (left). For the best match, there was overall good agreement concerning the path of wave propagation. However, the attenuation of the wave propagation was poorly modelled. This is possibly due to the sizes of the modelled grains being too small. Furthermore, the quadratic arrangement of the grid cells makes their edges either parallel or perpendicular to the incident wave minimizing mode conversion effects.

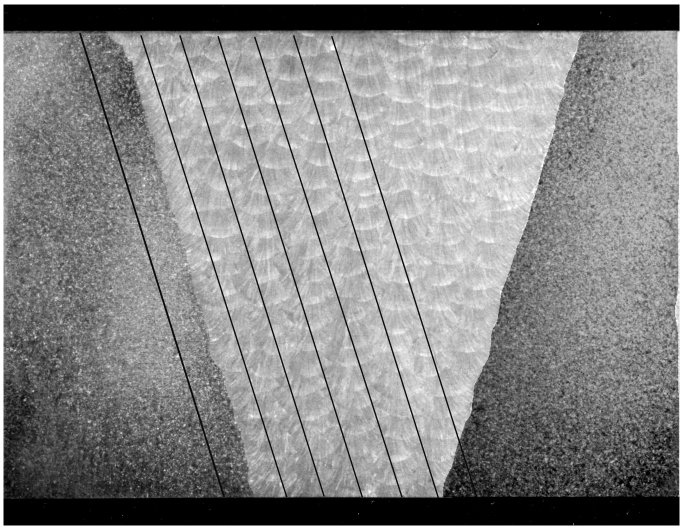

Figure 6.5: Illustration of the original weld together with the lines indicating the different cuts of the weld copies. The transmitter is placed on the leftmost line, while the receiver is placed on the opposite parallel cut for each weld copy.

6.3 Wave propagation in an austenitic weld

In this section, results from simulations of wave propagation in two welds are presented. The aim is to illustrate how the different types of waves are effected by the modelled weld structures. Following these is the A-scan in the case of a vertical crack positioned at the root in one of the welds. The A-scan for the equivalent "isotropic weld", i.e. the weld with the corresponding isotropic material is presented in order to estimate the differences between the two material assumptions.

6.3.1 Simulation of the transducer sound field in two welds

The grain structure of the first weld considered is shown in Fig. 6.6, with model parameters given in the legend. As seen, the weld root is quite narrow and the sloping boundaries are at larger angles to vertical compared to the weld in the last section. A similar weld has been considered in [47, 59] although with a different set of elastic parameters.

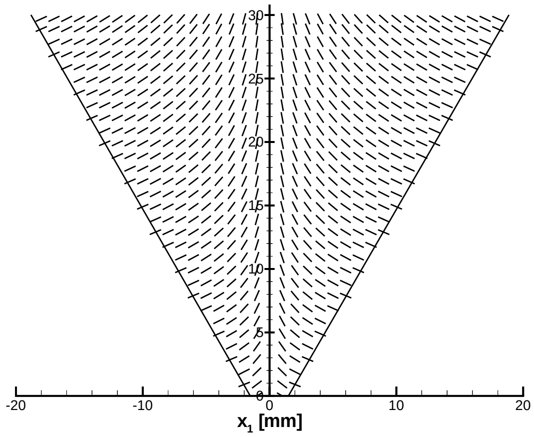

Figure 6.6: Grain structure of modelled weld. $D_1 = D_2 = 1.5\,\mathrm{mm}$ and $\alpha_1 = \alpha_2 = 30°$. $T_1 = T_2 = 0.57$ and $\eta = 0.97$. Weld material is X 6 CrNi 18 11.

Fig. 6.7 shows the wave field from a 2 MHz 45° SV transducer through the weld structure in Fig. 6.6 placed in isotropic austenite for different time steps. A transducer covering the whole weld surface has been used to ensure inspection of the entire area. An attempt has been made to identify the most important qSV waves in the weld. The transducer generated SV wave at the surface starts out as wave (1) in the isotropic medium and becomes wave (2) in the left half of the weld with an angle apparently similar to the angle in the isotropic medium, i.e. 45°. As time progresses, part of the wave (2) gets refracted back to wave (1). At the weld centerline, wave (2) results in a reflected wave (5) as well as a transmitted wave (4) while wave (2) continues as wave (3). As seen from the last picture at time $t = 14\,\mu\mathrm{s}$, the wave transmitted through the entire weld is essentially wave (3) and (4). Overall, it must be concluded, that the SV wave is heavily influenced by this weld structure, at least compared to the L wave and SH wave considered in the following.

Fig. 6.8 shows the wave propagation in the same medium as above but with a 2 MHz 45° SH transducer (for example from an EMAT or a piezoelectric transducer glued to the medium). It is immediately seen, that the SH wave is much less affected by the weld structure. The center region of the weld seems to be influencing the wave the most, resulting in small bends along the wave front of the transmitted wave.

Fig. 6.9 shows the same situation as above but for a 45° L wave. As in the SH case, the qL wave does not appear to be particularly influenced by the weld structure. There is a small bending across the transmitted wave and overall it appears as if the original angle of 45° has been retained. The simultaneously generated qSV wave at the transducer results in a rather complex picture of scattered qSV waves (as in the first example) behind the qL wave front.

The final example for this structure is shown in Fig. 6.10, where a 0° transducer is considered. In the case of wave fronts with a 0° wave vector, the centerline may act as a wave guide in the sense of beam convergence here. To appreciate this, consider Fig. 3.3 or

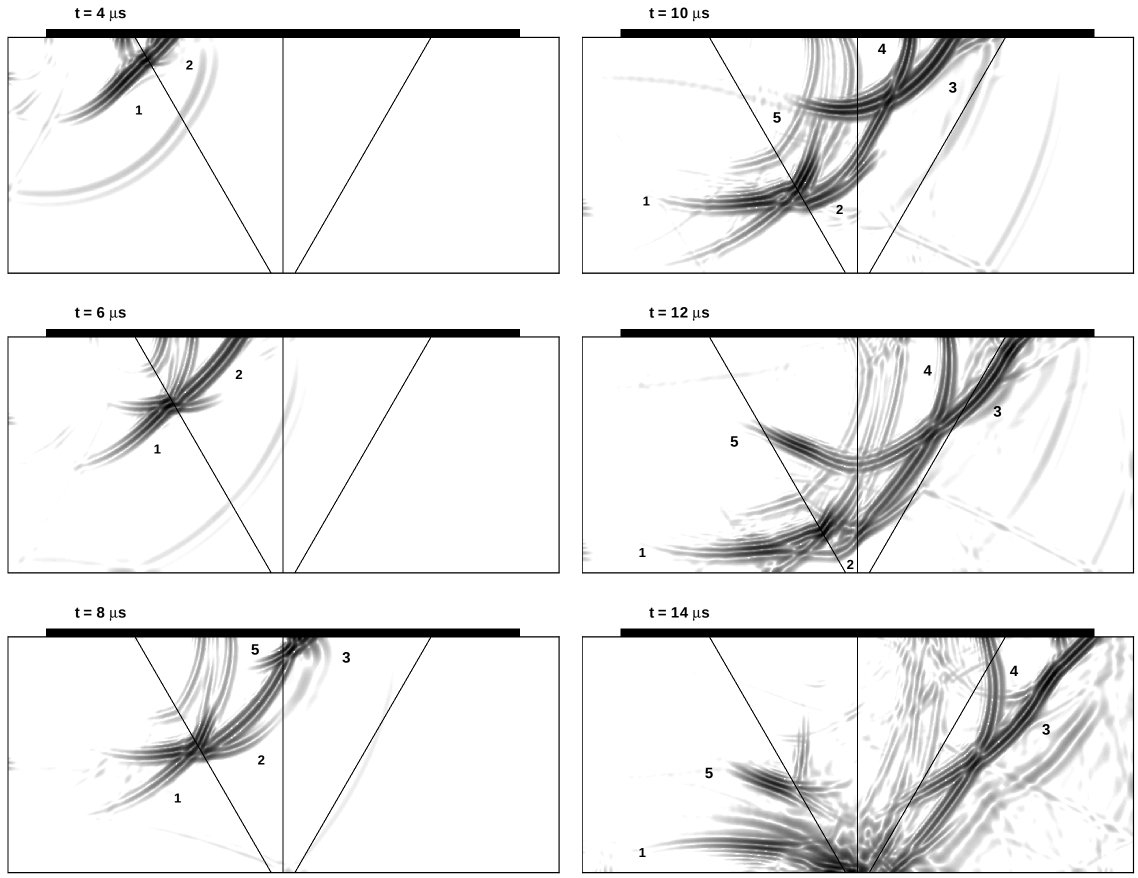

Figure 6.7: Wave propagation through the weld shown in Fig. 6.6 for different timesteps. The transducer signal is a 45° SV wave with a pulse signal $f(t;2)$ and $f_0 = 2\,\mathrm{MHz}$. Dimensions are $70\,\mathrm{mm} \times 30\,$ mm. Logarithmic scale from 0 dB (black) to -40 dB (white) with 25 levels. $(\Delta x, \Delta t) = (10^{-4}\,\mathrm{m}, 10^{-8}\,\mathrm{s})$.

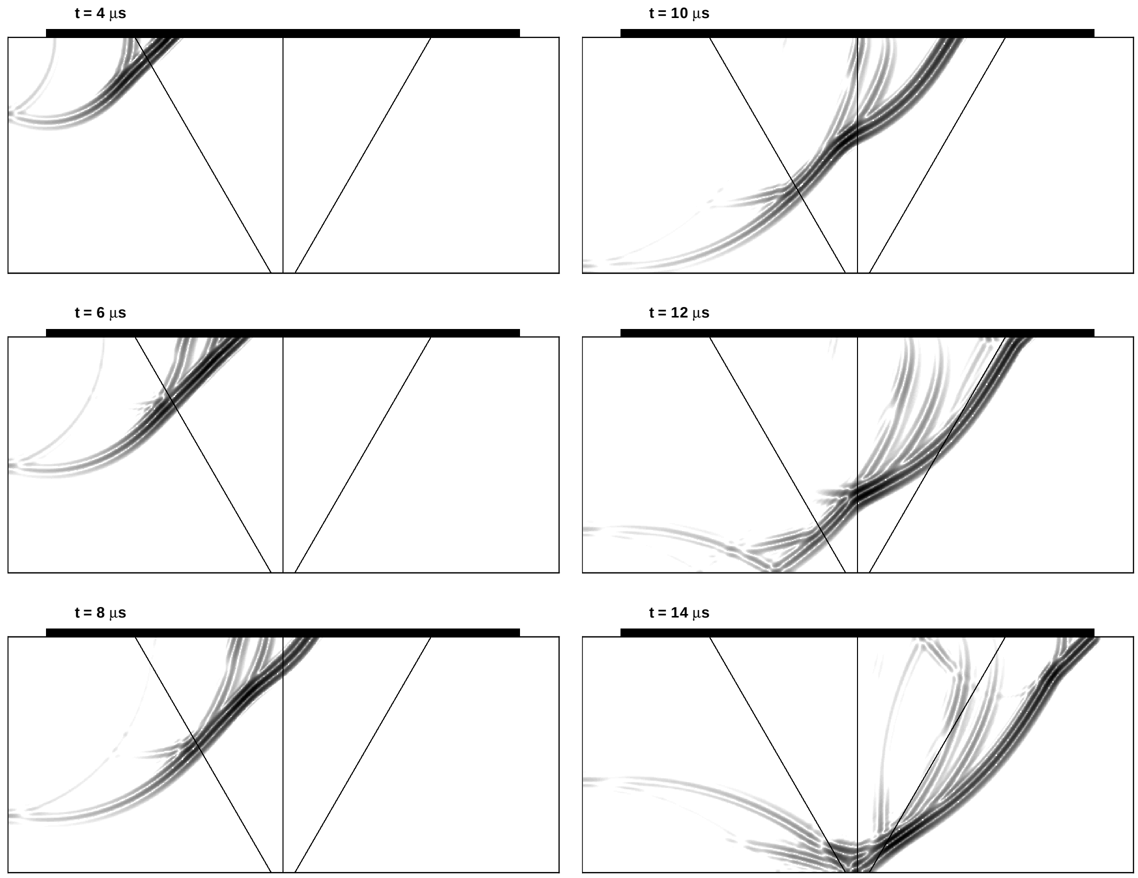

Figure 6.8: Wave propagation through the weld shown in Fig. 6.6 for different timesteps. The transducer signal is a 45° SH wave with a pulse signal $f(t;2)$ and $f_0 = 2\,\mathrm{MHz}$. Dimensions are 70 mm × 30 mm. Logarithmic scale from 0 dB (black) to -40 dB (white) with 25 levels. $(\Delta x, \Delta t) = (10^{-4}\,\mathrm{m}, 10^{-8}\,\mathrm{s})$.

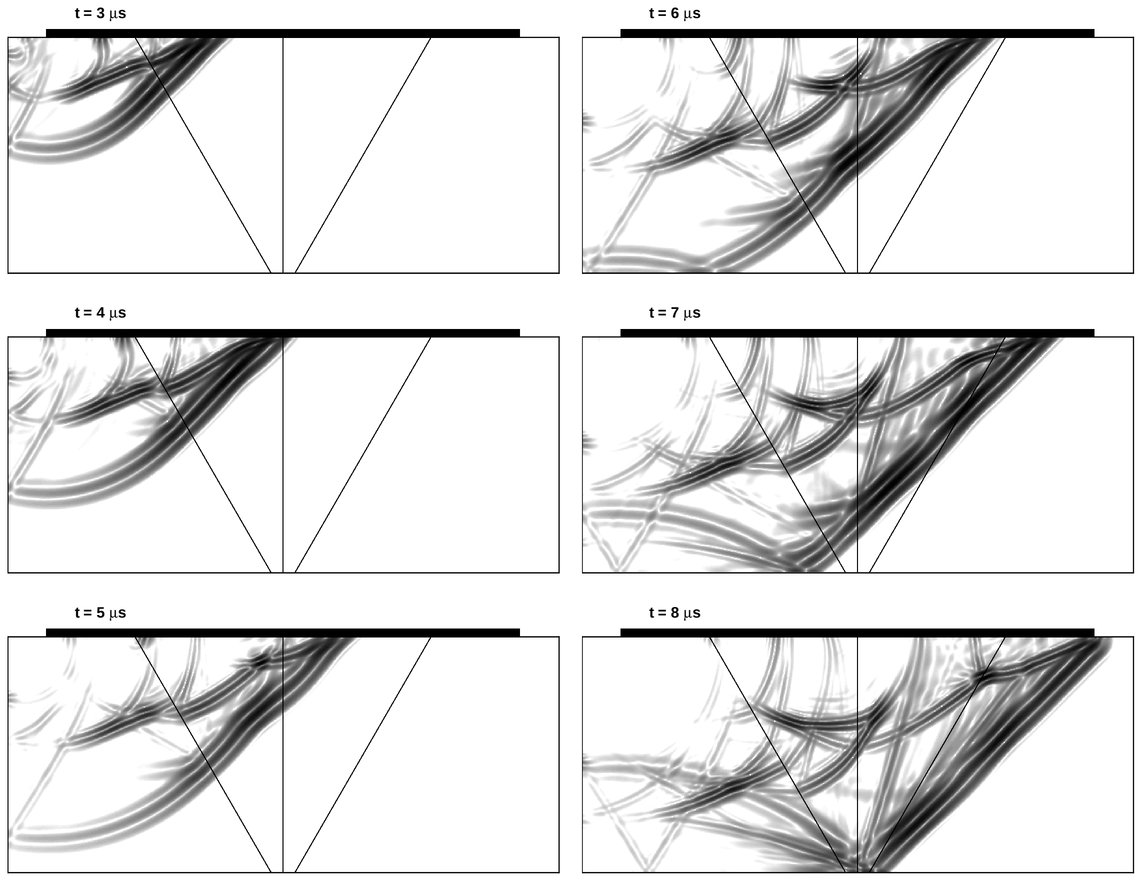

Figure 6.9: Wave propagation through the weld shown in Fig. 6.6 for different timesteps. The transducer signal is a 45° L wave with a pulse signal $f(t;2)$ and $f_0 = 2\,\mathrm{MHz}$. Dimensions are $70\,\mathrm{mm} \times 30\,\mathrm{mm}$. Logarithmic scale from 0 dB (black) to -40 dB (white) with 25 levels. $(\Delta x, \Delta t) = (10^{-4}\,\mathrm{m}, 10^{-8}\,\mathrm{s})$.

Fig. 3.4 (the two figures are similar for X 6 CrNi 18 11). At the centerline, the symmetry axis is vertical (parallel to the wave vector), while in the vicinity of the centerline, the symmetry axis makes a small angle (positive or negative) to vertical. Due to the convex form of the qL slowness curve, the energy vectors on both sides of the centerline are thus directed towards it. This is purely an anisotropic phenomenon, and is seen on the different plots in the figure, especially for the wave lacking behind the front wave.

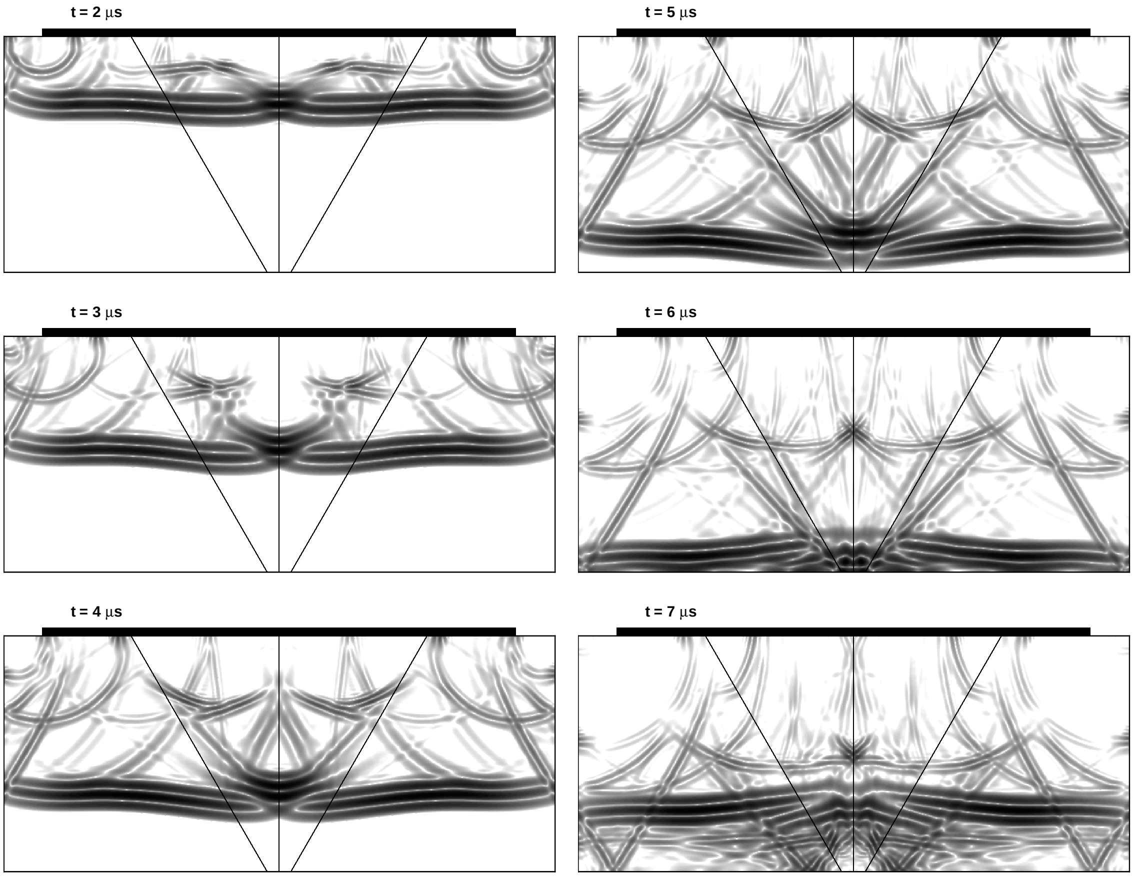

Figure 6.10: Wave propagation through the weld shown in Fig. 6.6 for different timesteps. The transducer signal is a 0° L wave with a pulse signal $f(t;2)$ and $f_0 = 2\,\mathrm{MHz}$. Dimensions are 70 mm × 30 mm. Logarithmic scale from 0 dB (black) to -40 dB (white) with 25 levels. $(\Delta x, \Delta t) = (10^{-4}\,\mathrm{m}, 10^{-8}\,\mathrm{s})$.

To investigate the effect of the weld structure and geometry on the wave propagation, simulations have furthermore been carried out using the weld model in Fig. 6.1 and Fig. 6.3 (left). Concerning the macrograph, only the lower half (3 cm) of the specimen is considered in the following. Fig. 6.11 shows the situation of a 45° SV wave incident upon the weld. As in the above case, the qSV waves are heavily influenced by the weld structure, and the most important qSV waves have been identified as above.

Fig. 6.12 shows the situation of a 45° SH wave. Again, the SH wave is much less affected by the weld structure, and the transmitted wave with an almost plane wave front is even less distorted than the SH wave in previous weld.

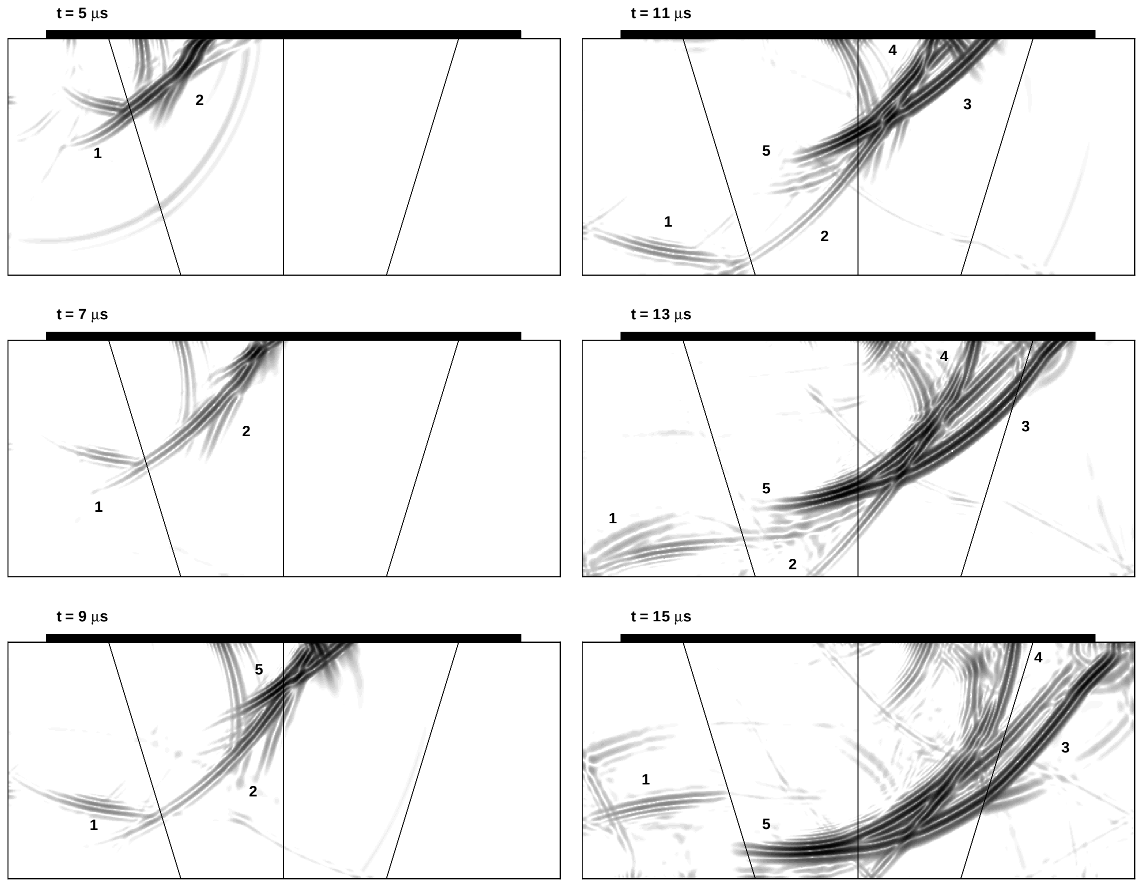

Figure 6.11: Wave propagation through the weld shown in Fig. 6.3 for different timesteps. The transducer signal is a 45° SV wave with a pulse signal $f(t;2)$ and $f_0 = 2\,\mathrm{MHz}$. Dimensions are $70\,\mathrm{mm} \times 30$ mm. Logarithmic scale from 0 dB (black) to -40 dB (white) with 25 levels. $(\Delta x, \Delta t) = (10^{-4}\,\mathrm{m}, 10^{-8}\,\mathrm{s})$.

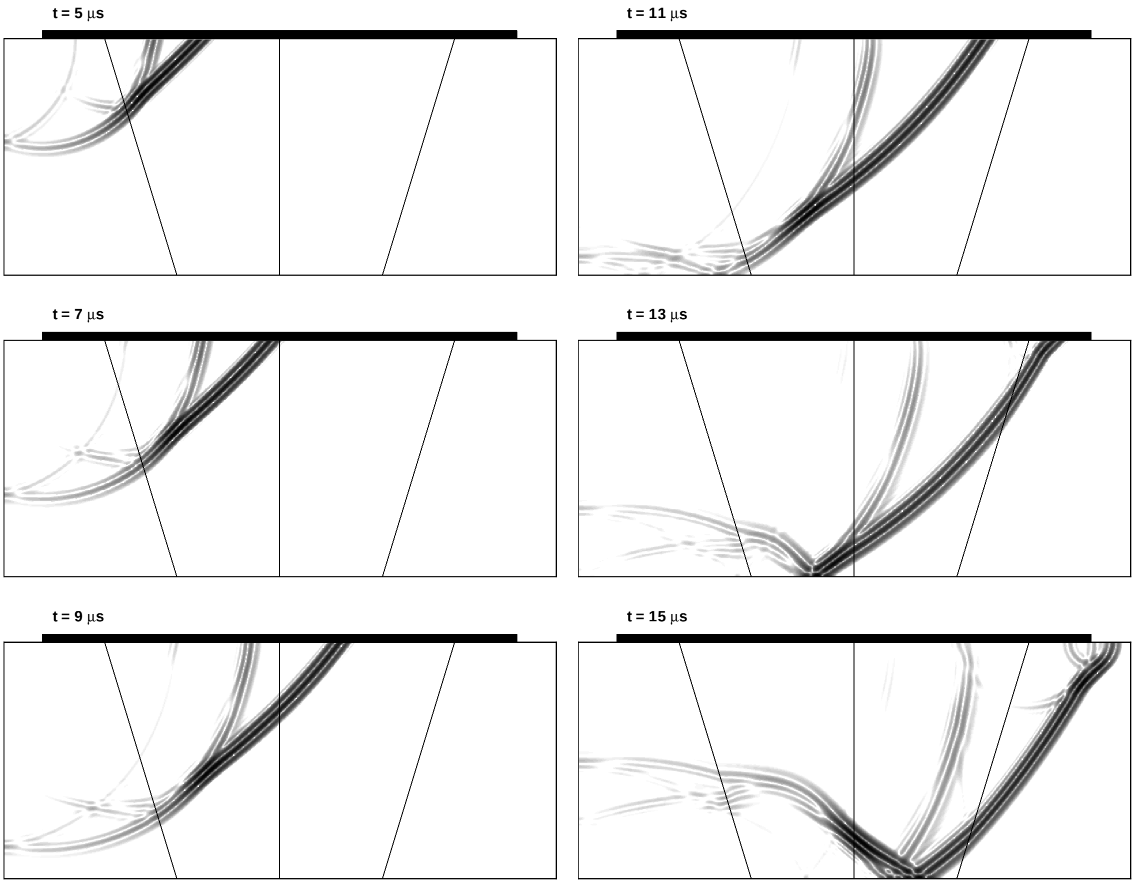

Figure 6.12: Wave propagation through the weld shown in Fig. 6.3 for different timesteps. The transducer signal is a 45° SH wave with a pulse signal $f(t;2)$ and $f_0 = 2\,\mathrm{MHz}$. Dimensions are 70 mm × 30 mm. Logarithmic scale from 0 dB (black) to -40 dB (white) with 25 levels. $(\Delta x, \Delta t) = (10^{-4}\,\mathrm{m}, 10^{-8}\,\mathrm{s})$.

The final example for a 45° L wave is shown in Fig. 6.13. Again, the qL wave is hardly affected by the weld structure and even less than the qL wave in the previous weld. The qSV wave also in this example results in a rather complex wave pattern behind the qL wave front.

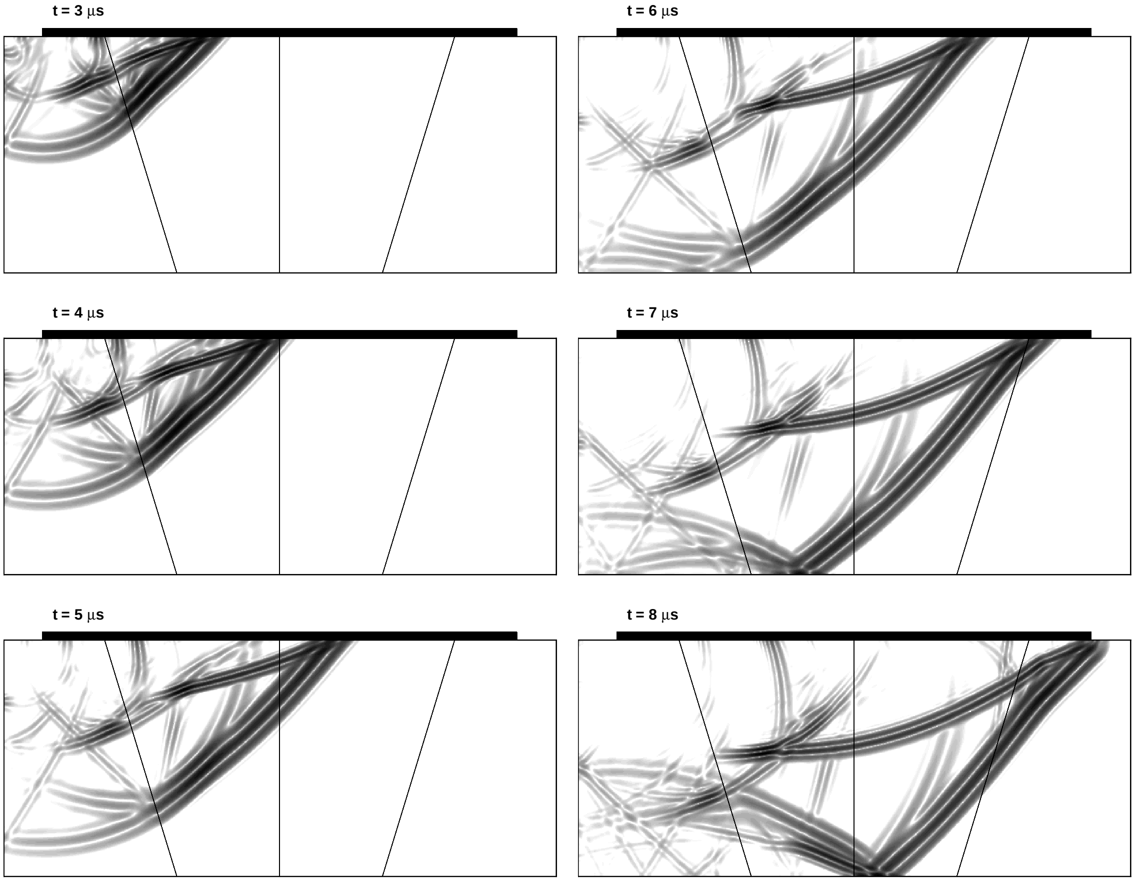

Figure 6.13: Wave propagation through the weld shown in Fig. 6.3 for different timesteps. The transducer signal is a 45° L wave with a pulse signal $f(t;2)$ and $f_0 = 2\,\mathrm{MHz}$. Dimensions are 70 mm × 30 mm. Logarithmic scale from 0 dB (black) to -40 dB (white) with 25 levels. $(\Delta x, \Delta t) = (10^{-4}\,\mathrm{m}, 10^{-8}\,\mathrm{s})$.

In this subsection, the wave propagation through two different weld structures has been simulated for different types of transducers. Overall it must be stated for both structures, that the incident SV wave is by far the most affected wave type, while the two other wave types (L and SH) are only affected a little. The major influence seems to take place at the two sloping boundaries as well as at the centerline. Concerning the two welds, the first weld with a narrow weld root and large (of the two weld examples) sloping angles resulting in a large angle of incidence to the weld ($45° + 30° = 75°$ for the first weld and $45° + 17° = 62°$ for the second), affected the different wave types the most. The first weld being of smaller extent has a larger change of symmetry axis orientation than does the second weld. This may explain the larger influence.

As a final point, it is noted that no backscattering is observed at the grain boundaries in the simulations. This may be due to the fact that each small grid cell in the numerical approach has acted as a grain. Therefore only very small changes in symmetry axis orientation occurs from grain to grain according to (6.1). These grain-to-grain changes might be so small, that no energy is reflected backwards, instead all the energy is transmitted. To circumvent this problem, a better model of the grain geometry and extent must be incorporated into the model.

6.3.2 A-scan from vertical crack at the weld root

In this subsection, the A-scan signal from a vertical backwall surface crack in a weld is modelled using the weld geometry and structure as shown in Fig. 6.1 and Fig. 6.3 (left) respectively. Based on the results of the last subsection, a 45° L transducer will be used as transmitter and receiver.

The problem is investigated in two ways. First, in a real NDT situation it might be necessary as a first step simply to consider the weld as being isotropic and homogeneous due to lack of further information about the weld. We shall also do this as a first approach and obtain an A-scan in the case of an isotropic, homogeneous austenite weld placed in isotropic ferritic steel. In the second approach, the full anisotropic inhomogeneous model is applied to the weld and the corresponding A-scan is obtained. Based on the two A-scans, it is possible to estimate "the error" made in considering an isotropic, homogeneous weld relative to a more elaborate model such as the one described earlier in this chapter.

In the first approach, the base metal is (isotropic) ferritic steel, while the weld consists of isotropic austenite, see Tab. 2.1, page 20. The corresponding simulations are shown in Fig. 6.14 for different timesteps. As seen in the first few steps, the two materials are quite similar such that almost all the energy is transmitted into the weld. At time $t = 10\,\mu$s, the longitudinal diffracted wave (DL) and the diffracted transverse wave (DT) at the upper crack tip are observed. The incident longitudinal wave is mainly mode converted at the crack from where it propagates towards the back wall. Here it is mode converted back to a longitudinal wave propagating back towards the receiver. This longitudinal corner echo (RL) is also seen. In the following timesteps these three relevant waves are detected at the receiver. The corresponding A-scan is shown in Fig. 6.16 (top). The amplitude is relative to the echo from the reference SDH with center at 20 mm and diameter 8 mm as considered in section 5.3.2. From the y-axis the maximum relative amplitude is seen to be -6.4 dB obtained from the longitudinal echo at time $t = 19\,\mu$s.

In the second approach, the weld is considered as being anisotropic and inhomogeneous as previously described. The corresponding simulations are shown in Fig. 6.15. The effect of beam skewing is clearly seen in the first two timesteps. The qL wave is seen to propagate downwards toward the weld root although the wave front still makes an angle of approximately 45° with vertical, compare with the same timesteps in the previous figure. Due to this beam skewing, the main part of the qL wave actually reaches the back first, from where it is reflected towards the crack. Here it is reflected back towards the receiver. This wave (RqL) is first identified at time $t = 12\,\mu$s. Due to the beam skewing a weaker part of the qL wave hits the upper crack tip with the result that the diffracted echoes have such low amplitudes, that they cannot be identified on the plots. For later timesteps, the reflected qL wave is detected by the receiver. The resulting A-scan is shown in Fig. 6.16 (bottom). As seen, only the reflected qL wave, arriving a bit earlier than the longitudinal wave in the first case, can be identified with certainty. For this case, the maximum relative

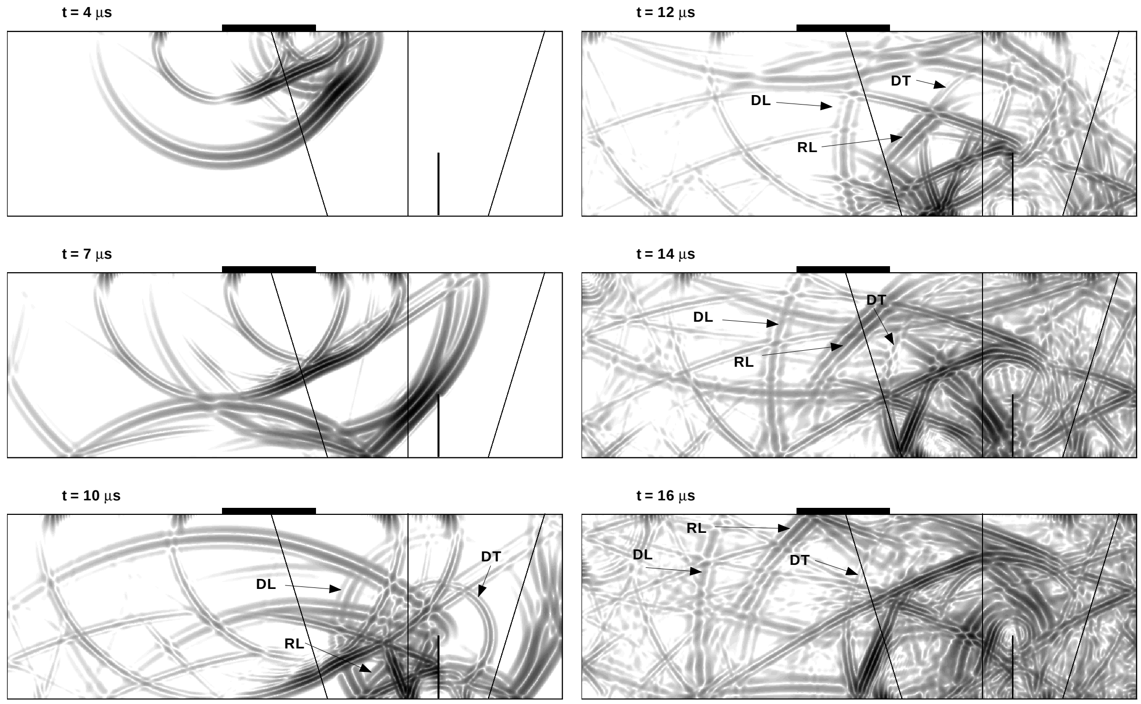

Figure 6.14: Wave propagation through an homogeneous isotropic austenite weld with geometry as in Fig. 6.1 for different timesteps. Base metal is ferritic steel. The transducer signal is a 45° L wave with a pulse signal $f(t;2)$ and $f_0 = 2\,\mathrm{MHz}$. Transducer width is 15 mm. Dimensions are 90 mm × 30 mm. Height of vertical crack is 10 mm and width is 0.1 mm. Crack is placed 5 mm from weld centerline. Logarithmic scale from 0 dB (black) to -45 dB (white) with 25 levels. $(\Delta x, \Delta t) = (10^{-4}\,\mathrm{m}, 10^{-8}\,\mathrm{s})$.

amplitude is -12.7 dB.

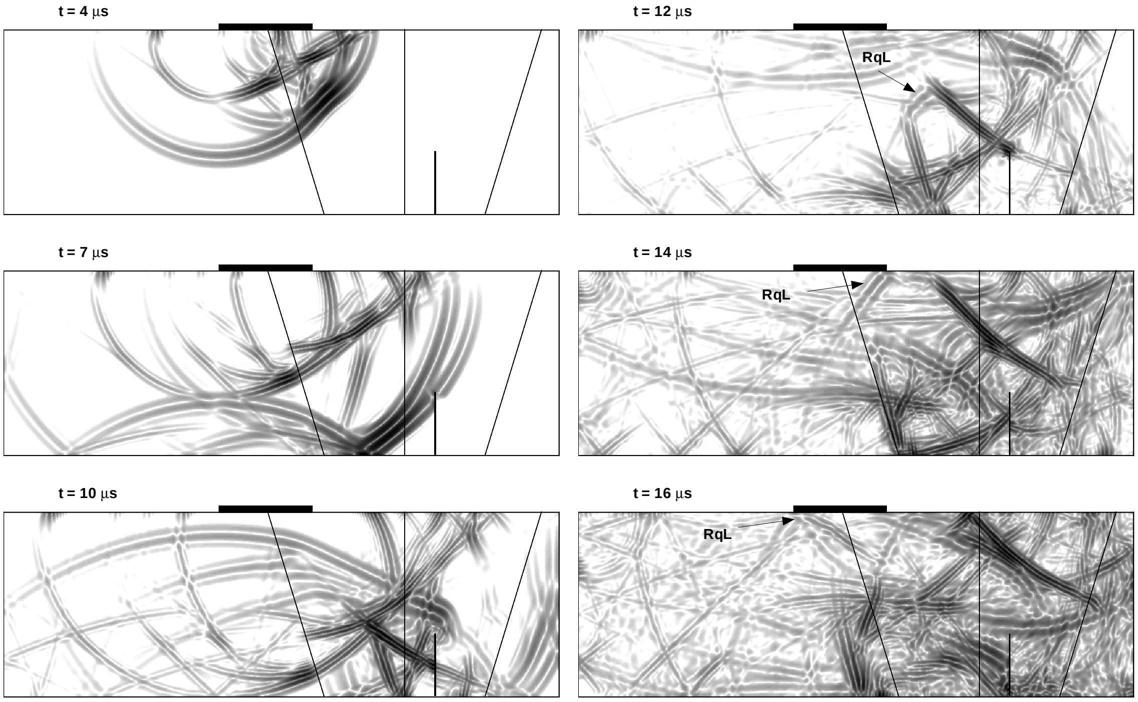

Figure 6.15: Wave propagation through an inhomogeneous anisotropic austenite weld with geometry as in Fig. 6.1 and structure as in Fig. 6.3 (left) for different timesteps. Base metal is ferritic steel. The transducer signal is a 45° L wave with a pulse signal $f(t;2)$ and $f_0 = 2\,\text{MHz}$. Transducer width is 15 mm. Dimensions are 90 mm × 30 mm. Height of vertical crack is 10 mm and width is 0.1 mm. Crack is placed 5 mm from weld centerline. Logarithmic scale from 0 dB (black) to -45 dB (white) with 25 levels. $(\Delta x, \Delta t) = (10^{-4}\,\text{m}, 10^{-8}\,\text{s})$.

We may try to summarize the observations made for this weld structure. As expected, the strongest detected signal in both cases is due to a longitudinal wave. However, in the second case, this wave is of qL nature, at it arrives approximately $0.4\,\mu\text{s}$ earlier. The path taken by the qL wave in the second case is also different due to beam skewing. As opposed to the isotropic case, it first reaches the back wall, from where it is reflected towards the crack. As mentioned in earlier chapters, this is a typical effect of anisotropic materials where, although the detected results are similar, the sound paths in the two cases are different. In this example it is not critical. However, in the worst case it may result in wrong conclusions drawn about the position and size of material defects. Finally, in the second case, the diffracted echoes are not strong enough to be detected by the receiver. This may indicate that methods based on diffraction echoes such as TOFD (Time Of Flight Diffraction), which is used for sizing vertical defects based on diffraction echoes from the upper and lower tips, may fail for such complex materials. Preferably, such numerical investigations should be carried out for each specific weld (or any other complex material), as it is difficult to make general statements about these issues.

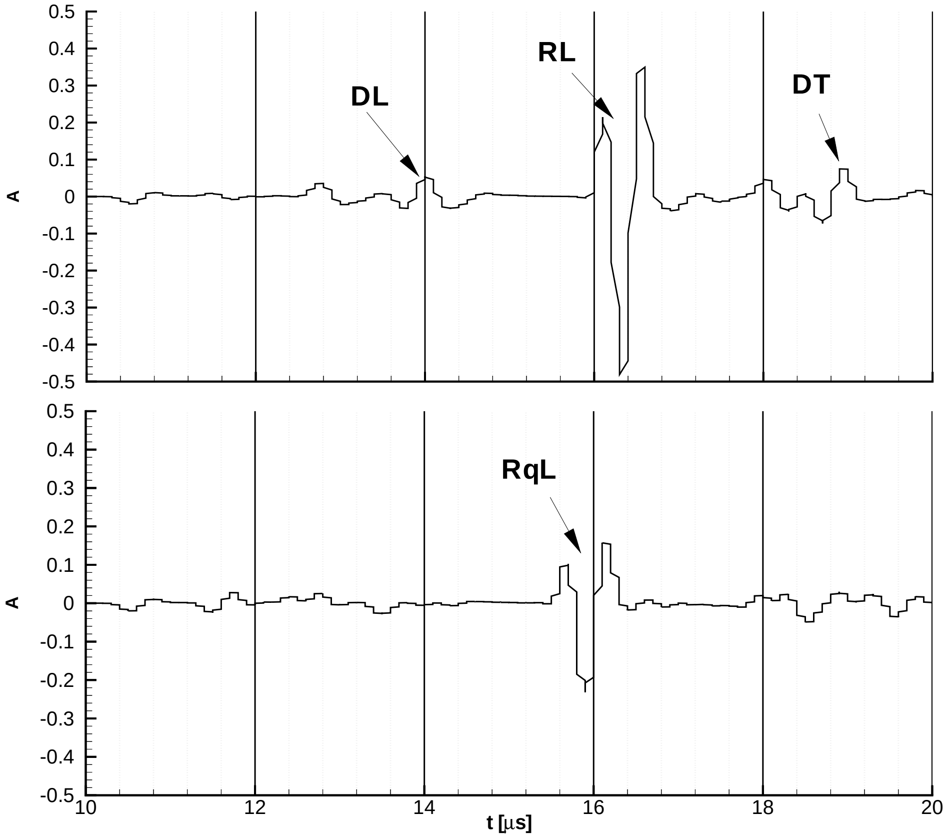

Figure 6.16: A-scans from a vertical crack in an isotropic austenitic weld (top) and an inhomogeneous anisotropic austenitic weld (bottom) using the weld structure in Fig. 6.3 (left). Corresponding simulations are found in Fig. 6.14 and Fig. 6.15 respectively.